

Research Article

Open Access

F. Lang*, A. Juma, V. Somsongkul, T. Dittrich, M. Arunchaiya

Rutherford Backscattering Spectroscopy of Mass Transport by Transformation of PbI_2 into $\text{CH}_3\text{NH}_3\text{PbI}_3$ within np-TiO_2

Abstract: Mass transport during transformation of PbI_2 infiltrated in nanoporous TiO_2 into $\text{CH}_3\text{NH}_3\text{PbI}_3$ has been investigated by Rutherford backscattering spectroscopy (RBS). Fast initial reaction kinetics were confirmed using optical ex-situ and in-situ measurements. Mapping with energy dispersive X-ray spectroscopy of the cross section of samples revealed a homogeneous PbI_2 infiltration in nanoporous TiO_2 before transformation but an accumulation of Pb and I at the surface after transformation, in accordance with a depletion of Pb and I in a near surface region. Quantitative depth profiles of Pb and I were obtained from RBS analysis. An instant degradation of $\text{CH}_3\text{NH}_3\text{PbI}_3$ to PbI_2 and volatiles upon ion radiation was found. The concentration profiles of Pb could be simulated with a one dimensional diffusion model taking into account an effective diffusion coefficient of Pb in the nanocomposite (about $1.5 \cdot 10^{-11} \text{ cm}^2/\text{s}$) as well as a parameter considering frazzling at the surface due to formation of crystallites.

Keywords: $\text{CH}_3\text{NH}_3\text{PbI}_3$, PbI_2 , nanoporous- TiO_2 , Rutherford backscattering spectroscopy (RBS), transport of lead, degradation

DOI 10.2478/hyma-2014-0002

Received September 30, 2014; accepted November 25, 2014

*Corresponding author: **F. Lang:** Helmholtz-Zentrum Berlin für Materialien und Energie GmbH, Hahn-Meitner-Platz 1, 14109 Berlin, Germany, E-mail: felix.lang@helmholtz-berlin.com

A. Juma, V. Somsongkul, T. Dittrich: Helmholtz-Zentrum Berlin für Materialien und Energie GmbH, Hahn-Meitner-Platz 1, 14109 Berlin, Germany

A. Juma: Tallinn University of Technology, Department of Materials Science, Ehitajate tee 5, Tallinn 19086, Estonia

V. Somsongkul, M. Arunchaiya: Department of Materials Science, Faculty of Science, Kasetsart University, Bangkok 10900, Thailand

1 Introduction

The hybrid perovskite methylammonium lead iodide ($\text{CH}_3\text{NH}_3\text{PbI}_3$) combines a band gap between 1.5 eV and 1.6 eV [1,2], a high absorption coefficient of $\alpha \sim 10^4 \text{ cm}^{-1}$ at 600 nm [3] and ambipolar diffusion lengths of around 100 nm [4,5]. The combined properties allowed solar cell efficiency boosting from e.g. 3 % in 2009 [6] to over 15 % in 2013 [7,8] and 16.2 % [9] / 17.9 % [10] in 2014. Perovskite thin film preparation can be drawn back to four major techniques: 1st a co-evaporation of organic and inorganic precursors [8], 2nd spin coating from dissolved perovskite [11–17], 3rd in a sequential deposition process [7,18–20] and 4th using spray deposition [21,22]. Individual advantages enabling high efficiency and cost-effective processing are still under debate. Discussed effects range from reliable control over morphology [7,19,20,23], influence on material properties [24,25] to the formation of passivated interfaces [26–28].

The key reaction in the sequential deposition is the transformation reaction of an inorganic precursor layer such as PbI_2 to the final $\text{CH}_3\text{NH}_3\text{PbI}_3$ by dipping into an organic precursor solution containing $\text{CH}_3\text{NH}_3\text{I}$. Providing high surface to volume ratio, observed reaction kinetics are fast (tens of seconds) [7]. The underlying mechanism is believed to be an insertion reaction, accelerated by the layered PbI_2 crystal structure [7,18,29]. Recently a model of the intercalation process on a molecular level was proposed based on in-situ photoluminescence (PL) studies of the intercalation depending on precursor concentration (3 – 15 mM), solvent polarity and size of the organic component [29]. The proposed model starts with transformation of the first PbI_2 layer to an incomplete PbI_4^{2-} network, while created interstices allow organic intercalation and consecutive conversion of underlying layers [29]. Intercalation kinetics matched the Johnson-Mehl-Avrami-Kolmogorov (JMAK) model [29].

The objective of this work was the investigation of the

transformation reaction from PbI_2 to $\text{CH}_3\text{NH}_3\text{PbI}_3$ within a np-TiO₂ host scaffold as used for perovskite solar cells. The used high $\text{CH}_3\text{NH}_3\text{I}$ solution concentration (ca. 63 mM) further is expected to cause steric hindrance from many molecules binding, thus preventing and/or alternating the intercalation mechanism [29]. Reaction kinetics were first investigated optically using ex-situ and in-situ absorption measurements. Reported reaction kinetics [7] were confirmed. Knowledge about Pb and I distribution within the porous matrix is essential to investigate ongoing processes. Therefore, energy dispersive X-ray (EDX) spectroscopy mapping of prepared cross sections was performed on transformed $\text{CH}_3\text{NH}_3\text{PbI}_3$ and the PbI_2 precursor. Rutherford backscattering spectroscopy (RBS) further was used to gain a quantitative depth profiling of Pb and I. The TiO₂ host matrix hereby provided (i) the needed surface to volume ratio for $\text{CH}_3\text{NH}_3\text{PbI}_3$ transformation, (ii) a surface reference point for RBS, whereas (iii) Ti was sufficiently light and thus well separated from Pb and I in RBS spectra. Regarding degradation of $\text{CH}_3\text{NH}_3\text{PbI}_3$ by the used He⁺ ions, attention has been paid to the orthogonal e⁻ and He⁺ analysis beam direction of the two used techniques EDX and RBS. As a remark, hybrid perovskites in general may be highly air sensitive [24,30] while specifically $\text{CH}_3\text{NH}_3\text{PbI}_3$ decomposition in presence of moisture [31], Lewis bases [32] or X-rays [33] has been reported recently.

2 Experimental Details

2.1 Sample Preparation

Methyl ammonium iodide $\text{CH}_3\text{NH}_3\text{I}$ was synthesized similarly to a reported method [1,34]. In short the methyl ammonium iodide salt was synthesized by reaction of 30 ml methylamine (40 wt% in H₂O, Aldrich) with 30 ml of hydroiodic acid (57 wt%, un-stabilized in H₂O, Aldrich). The raw product was recovered using a rotary evaporator, washed extensively with diethyl ether and finally purified by two solvent recrystallization. After drying at 60°C in vacuum (78 h) the compound was stored under inert gas. A three μm thick nanoporous (np) TiO₂ scaffold was prepared for EDX and RBS measurements by screen printing a paste containing TiO₂ nanoparticles with a diameter of 25 nm on cleaned SnO₂:F substrates, first and fired at 450°C, second. Optical measurements were performed on a 320 nm thick np-TiO₂ film obtained by spin-coating twice a TiO₂ nanoparticle solution (Solaronix D/SC) followed by calcination at 450°C for 30 min. In both cases calcination was repeated prior to usage. $\text{CH}_3\text{NH}_3\text{PbI}_3$

was prepared using the sequential deposition technique [7]. Therefore PbI_2 (Sigma Aldrich 99.98 %) was dissolved in DMF at various concentrations $c = 1 \text{ M}, 0.5 \text{ M}, 0.25 \text{ M}$ and infiltrated into np-TiO₂ by spin coating at 6500 r.p.m. for 90 s (5500 r.p.m./s). The solution temperature was kept at 70°C during the whole procedure. Obtained films were transferred into inert atmosphere (N₂) dried at 70°C for 30 min and subsequently dipped into $\text{CH}_3\text{NH}_3\text{I}$ solution in isopropanol ($c = 10 \text{ mg/ml}$). Dipping time was either varied or kept at 60 s. After immediate rinsing with isopropanol the films were dried at 70°C for 30 min. Figure 1 illustrates the model system used to investigate the transformation to $\text{CH}_3\text{NH}_3\text{PbI}_3$ within the np-TiO₂. As remark samples were prepared and transported in inert atmosphere, mounted in air (< 3 min) and directly transferred to vacuum in case of RBS, SEM and EDX measurements.

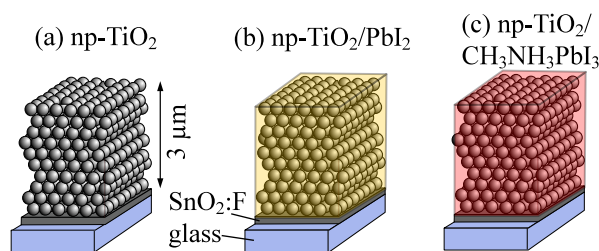


Figure 1: Sketch of used model system: (a) screen printed np-TiO₂, (b) after infiltration with PbI_2 and (c) after transformation to $\text{CH}_3\text{NH}_3\text{PbI}_3$ by dipping in $\text{CH}_3\text{NH}_3\text{I}$.

2.2 Analytical Methods

Spectral dependent transmission and reflection was measured using a Perkin Elmer Lambda 950 equipped with an integrating sphere. Light impinged from the glass side. Spectral dependent absorption was calculated accordingly. In-situ reaction dynamics were monitored measuring the change of transmission over time, using a fixed illumination from a red LED ($\lambda \sim 640 \text{ nm}$) and a silicon photodiode in direct geometry. Samples were placed in a cuvette before rapid injection of the $\text{CH}_3\text{NH}_3\text{I}$ solution. The change in absorbance was calculated from acquired data. SEM images of prepared surfaces and cross sections were taken with a Zeiss Leo 1530 Gemini scanning electron microscope with an in-lens detector at an acceleration voltage E_{HT} of 10 keV. EDX maps were acquired accordingly at $E_{\text{HT}} = 20 \text{ keV}$. Obtained data of the Pb (L edge), I (L edge) and Ti (K edge) were averaged horizontally and analyzed as bare counts versus vertical distance. Rutherford backscattering spectroscopy (RBS) was performed with ⁴He⁺ ions at an energy of 1.4 MeV. Measurements were

taken in Cornell geometry with (i) 0° incident angle and 168° scattering angle and (ii) 5° incident angle and 150° scattering angle. The used detector had a FWHM of 14 MeV. The ion beam current was ~ 4.1 nA. Measurements were taken with a total charge of incident ions of $6 \mu\text{C}$, thus measurement time was around 25 minutes. The dose Φ per measurement was $\sim 10^{15} \text{ cm}^{-2}$. The $^4\text{He}^+$ ion flux was $\sim 10^{16} \text{ cm}^{-2}\text{s}^{-1}$.

2.3 Analysis of RBS Spectra

In order to gain quantitative information about concentration profiles of Pb and I a multi-layer system was introduced and optimized recursively by forward simulation using the RBS analysis software SPEWA. Up to 20 layers with individual Pb, I, Ti and O concentration were optimized. Light elements such as N, C and H were neglected in both the RBS simulation and calculation of the stopping power. RBS simulation therefore may deviate from measurement data for unimportant channel numbers lower than 150, while the error in the stopping power was below 0.5 %. As remark, an Sn concentration of around 0.09 at% was considered in the simulation, based on the observed Sn diffusion from $\text{SnO}_2:\text{F}$ into TiO_2 during firing. Simulations were performed assuming an np- TiO_2 porosity of 50%, thus $N_{\text{TiO}_2} = 4.41 \cdot 10^{22} \text{ atoms/cm}^3$. The increase of the atomic density due to infiltration was considered as $N = N_{\text{TiO}_2} + N_{\text{PbI}_2}$ with $N_{\text{PbI}_2} = 2.41 \cdot 10^{22} \text{ atoms/cm}^3$. The stoichiometric ratio of Ti to O was fixed to 1:2 throughout the RBS analysis. The Pb and I ratio was first analyzed from the Pb and I edge intensity and then fixed in the further multi-layer system optimization. The optimized multi-layer system is an effective layer system.

Surface roughness and a depth dependent porosity were not taken into account for obtaining concentration profiles. However it is known that surface roughness and porosity influences RBS spectra [35,36], whereas a detailed consideration of related effects is practically impossible for complex systems. As remark, the surface roughness was estimated by crystallites formed at the surface. Resulting variances of concentrations and concentration profiles were estimated by varying the parameters of the multilayer systems for simulations of RBS spectra.

3 Results and Discussion

3.1 In-Situ and Ex-Situ Optical Characterization

Figure 2 shows spectral dependent absorption for np- TiO_2 infiltrated with $c(\text{PbI}_2) = 1 \text{ M}$ (0 s) and after dipping and drying for t_{dip} of 5, 20, 60 and 300 s. Absorption onsets are in accordance with the band gap of PbI_2 ($E_G(\text{PbI}_2) = 2.3 \text{ eV}$, $\lambda_G(\text{PbI}_2) \approx 539 \text{ nm}$) [37] and of the transformed $\text{CH}_3\text{NH}_3\text{PbI}_3$ ($E_G(\text{CH}_3\text{NH}_3\text{PbI}_3) = 1.6 \text{ eV}$, $\lambda_G(\text{CH}_3\text{NH}_3\text{PbI}_3) \approx 774 \text{ nm}$) [2]. The inset in Figure 1 shows the in-situ measured change in absorbance. Two regimes could be identified 1st a sharp onset until up to ~ 20 s and 2nd a quasi-saturation with slower increase. In analogy to [7] the absorbance kinetics were fitted using a bi-exponential function. Obtained decay times of $\tau_1 = 5.0 \text{ s}$ and $\tau_2 = 156 \text{ s}$ were similar to $\tau_1 = 5.0 \text{ s}$ and $\tau_2 = 109 \text{ s}$ as measured by [7] at 550 nm. In contrast however the slow process here still led to significant $\text{CH}_3\text{NH}_3\text{PbI}_3$ transformation, as seen in the absorption increase for $t_{\text{dip}} = 300 \text{ s}$. As a remark

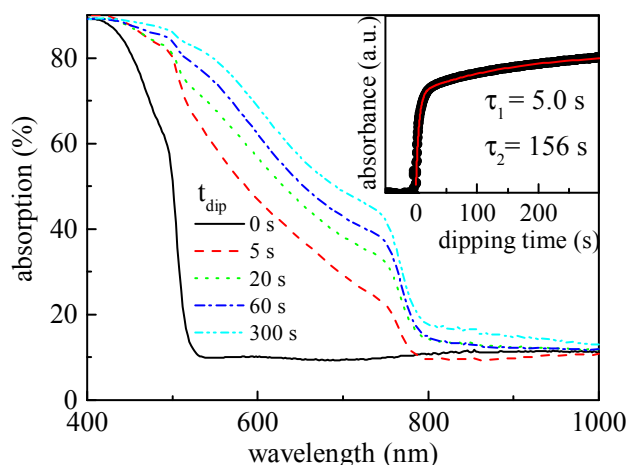


Figure 2: Spectral dependent absorption of 320 nm thick np- TiO_2 infiltrated with PbI_2 $c = 1 \text{ M}$ (0 s) and after various dipping times 20 s, 60 s and 300 s. Absorption was calculated from transmission and reflection measurements using an integrating sphere. Inset shows kinetic trace of in-situ absorbance, calculated from direct transmittance obtained by a silicon photodiode and a red LED (640 nm). Obtained decay times, as based on a bi-exponential fit (red line) are indicated.

the observed absorption feature of PbI_2 was present in all transformed samples although consequently reducing. We described the role of such unreacted PbI_2 upon charge separation elsewhere [27].

3.2 Morphology and Composition of Cross Sections

Figure 3 shows top view SEM images of (a) np-TiO_2 , (b) np-TiO_2 with infiltrated PbI_2 and (c) after transformation to $\text{CH}_3\text{NH}_3\text{PbI}_3$ by dipping for $t_{\text{dip}} = 60$ s. PbI_2 ($c(\text{PbI}_2) = 1$ M) infiltrated into the np-TiO_2 , no capping layer was formed. After transformation the surface was homogeneously covered with perovskite crystallites of diameter 130 ± 40 nm. The formation of surface crystallites as formed by or during sequential deposition is reported throughout literature [19,23,38–40].

Figure 4 shows cross sectional scanning electron microscope (SEM) images of the $3 \mu\text{m}$ thick used model system, (a) $\text{np-TiO}_2/\text{PbI}_2$ ($c(\text{PbI}_2) = 1$ M) and (c) after transformation to $\text{CH}_3\text{NH}_3\text{PbI}_3$ ($t_{\text{dip}} = 60$ s). PbI_2 was found to infiltrate completely. After transformation the formation of a dense perovskite capping layer with additional out sticking perovskite crystallites of larger size was observed, see Figure 1 (c). Horizontally averaged EDX maps are shown as bare counts versus vertical distance in Figure 4 (b) and (d). A rather homogeneous distribution of Pb and I in the np-TiO_2 host bulk with a slight depletion at the surface was found for $\text{np-TiO}_2/\text{PbI}_2$ Figure 4 (b). After transformation to perovskite (Figure 4 (c)) an accumulation of Pb and I was found at the surface, followed by a consistent depletion in a depth between $0.5 - 1 \mu\text{m}$. The found accumulation was in agreement with the formation of perovskite crystallites at the surface.

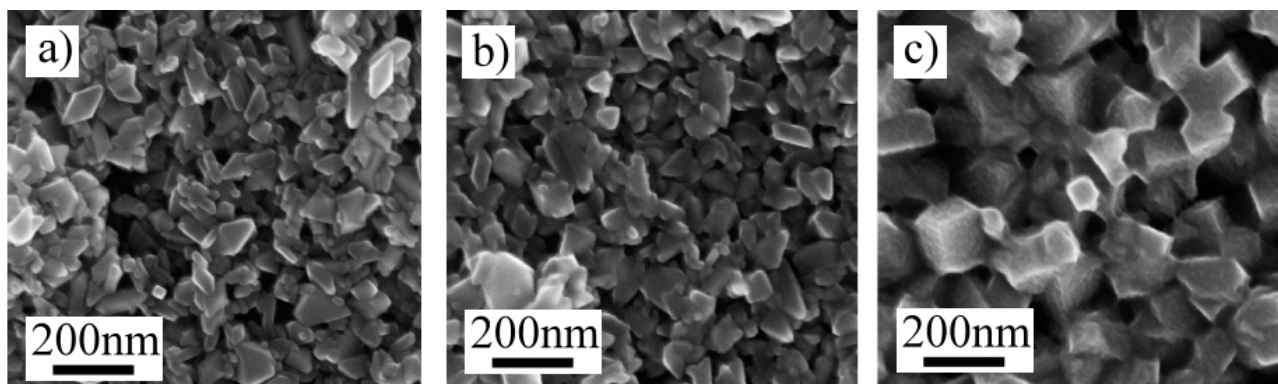


Figure 3: Top view SEM image of (a) np-TiO_2 , (b) np-TiO_2 with infiltrated PbI_2 and (c) after transformation to $\text{CH}_3\text{NH}_3\text{PbI}_3$ by dipping for $t_{\text{dip}} = 60$ s, $c(\text{PbI}_2) = 1$ M.

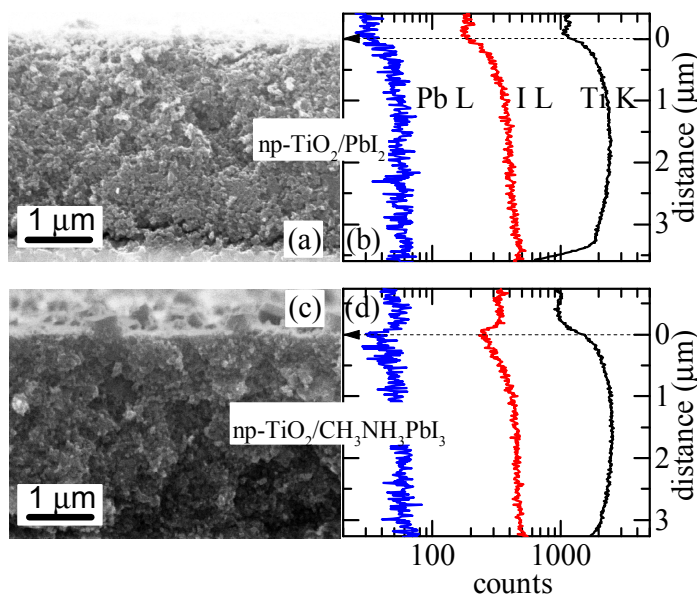


Figure 4: SEM images and corresponding EDX mapping of prepared cross sections for Pb, I and Ti of $\text{np-TiO}_2/\text{PbI}_2$ ($c = 1$ M) (a) and (b) as well as of $\text{np-TiO}_2/\text{CH}_3\text{NH}_3\text{PbI}_3$ as obtained for a dipping time of $t_{\text{dip}} = 60$ s (c) and (d). Arrows mark the np-TiO_2 surface, which was set to zero.

3.3 Stoichiometry Analysis by Rutherford Backscattering Spectroscopy

3.3.1 Degradation of $\text{CH}_3\text{NH}_3\text{PbI}_3$ by Ion Radiation

Figure 5 shows RBS measurements of the investigated model system: bare np-TiO_2 , after infiltration with PbI_2 and after transformation to $\text{CH}_3\text{NH}_3\text{PbI}_3$. Prior to analysis, the $\text{CH}_3\text{NH}_3\text{PbI}_3$ material stability during RBS measurements was tested by measuring twice, indicated as 1 and 2 measurement. A zoom in focuses on the lead and iodide peaks and further shows performed simulations, based on a confined stoichiometry of either PbI_3 or PbI_2 . Repeated measurements resulted in identical spectra. The simulation clearly revealed a stoichiometry of PbI_2 . The observation was in contrast to the expected $\text{CH}_3\text{NH}_3\text{PbI}_3$ stoichiometry of PbI_3 . A color change from black to yellow was observed locally on the $^4\text{He}^+$ beam spot after ion exposure. A $^4\text{He}^+$ ion radiation induced degradation mechanism from $\text{CH}_3\text{NH}_3\text{PbI}_3$ to PbI_2 (solid), CH_3NH_2 and HI (both volatile) is proposed. The new PbI_2 phase in contrast has higher radiation hardness [37]. In general ion projectiles with high kinetic energy will deposit energy by electronic interaction forming the so called ion track. In detail this includes a fast initial electronic ionization and excitation along the ion path with few nanometer in diameter, first and a subsequent energy conversion from electronic potential to atomic motion, second. Depending

on the charge-neutralization time and ionization density this conversion follows the coulomb-explosion, lattice-relaxation or electronic thermal-spike model [41,42]. Depending on the target electronic and thermal properties this may alter phase and target properties [41]. Well known effects are e.g. chemical modifications in polymers, starting from an electronic stopping power of $dE/dx \sim 0.26 \text{ keV/nm}$ [43] or morphological changes in mica, starting from $dE/dx \sim 5 \text{ keV/nm}$ [44]. In $\text{CH}_3\text{NH}_3\text{PbI}_3$ dE/dx is around 0.27 keV/nm [45]. The areal density of perovskite $\rho_A \sim 4 \cdot 10^{14} \text{ cm}^{-2}$ is smaller than the measurement dose Φ of $\sim 10^{15} \text{ cm}^{-2}$. Therefore the immediate and complete degradation of $\text{CH}_3\text{NH}_3\text{PbI}_3$ to PbI_2 requires a diameter of the latent ion track of a few tens of nm. Sophisticated experiments however are required for getting a reliable value for the diameter of the damaged region, the (latent) ion track and detailed interaction mechanisms.

The rapid $\text{CH}_3\text{NH}_3\text{PbI}_3$ degradation, induced by the analyzing beam however did not introduce significant error when analyzing the immobile Pb. Further analysis therefore was based on the Pb concentration profile. Additional and/or consequent surface blistering or porosity changes due to implanted He [46] or volatile degradation products was not observed in SEM analysis (top view, unpublished), first and neglected due to the present nanocomposite structure facilitating any outgassing, second.

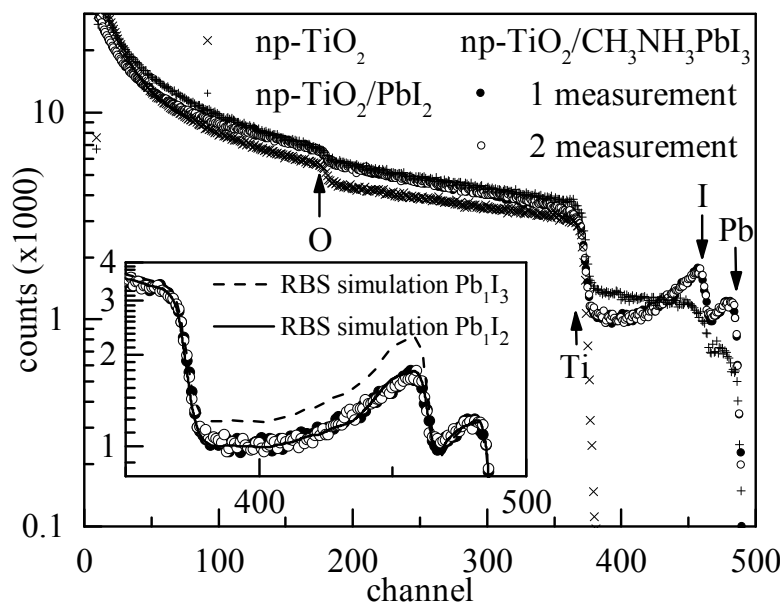


Figure 5: RBS spectra of investigated model system: np-TiO_2 , $\text{np-TiO}_2/\text{PbI}_2$ and $\text{np-TiO}_2/\text{CH}_3\text{NH}_3\text{PbI}_3$ for $c(\text{PbI}_2) = 0.25 \text{ M}$ and $t_{\text{dip}} = 60 \text{ s}$. Inset focuses on Pb and I peaks, analyzing the stability of RBS spectra upon multiple measurements. Circles present measurement data, while lines present RBS simulation based on the confined stoichiometry PbI_3 and PbI_2 . Used geometry (i).

3.3.2 Evaluation of Concentration Profiles

The RBS spectra presented in Figure 5 revealed a rather homogenous PbI_2 infiltration but an Pb and I accumulation at the surface in accordance with a depletion of Pb and/or I in the near surface region, around channel 400. As remark conceptually identical concentration profiles were observed after transformation to $\text{CH}_3\text{NH}_3\text{PbI}_3$ independent of the applied post treatment at 100°C, 140°C, 160°C and 20°C (unpublished). The observed accumulation therefore was an entire effect of the phase transformation to $\text{CH}_3\text{NH}_3\text{PbI}_3$.

A detailed analysis of the phase transformation from PbI_2 to $\text{CH}_3\text{NH}_3\text{PbI}_3$ is shown in Figure 6 for a fixed dipping time of $t_{\text{dip}} = 0$ s and $t_{\text{dip}} = 60$ s under variation of PbI_2

solution concentration $c(\text{PbI}_2) = 1$ M, 0.5 M, 0.25 M, Figure 6 (a), (b) and (c). Pronounced surface related Pb and I peaks were observed independent of $c(\text{PbI}_2)$, while the depletion around a depth of 400 nm becomes larger and more pronounced with decreasing $c(\text{PbI}_2)$.

Optimized multi-layer systems are shown in Figure 7 for $c(\text{PbI}_2) = 1$ M (a), 0.5 M (b) and 0.25 M (c). Open (closed) circles denote Pb concentration before (after) dipping for $t_{\text{dip}} = 60$ s. Figure 7 shows the obtained layer system without error bars.

In case of $\text{np-TiO}_2/\text{CH}_3\text{NH}_3\text{PbI}_3$ further surface layers of pure Pb and I had to be simulated. Obtained areal densities are: $c(\text{PbI}_2) = 1$ M, $N_{\text{surface}} = (0.93 \pm 0.3) \cdot 10^{15}$ at/cm², $c(\text{PbI}_2) = 0.5$ M, $N_{\text{surface}} = (0.57 \pm 0.3) \cdot 10^{15}$ at/cm² and $c(\text{PbI}_2) = 0.25$ M, $N_{\text{surface}} = (0.93 \pm 0.3) \cdot 10^{15}$ at/cm².

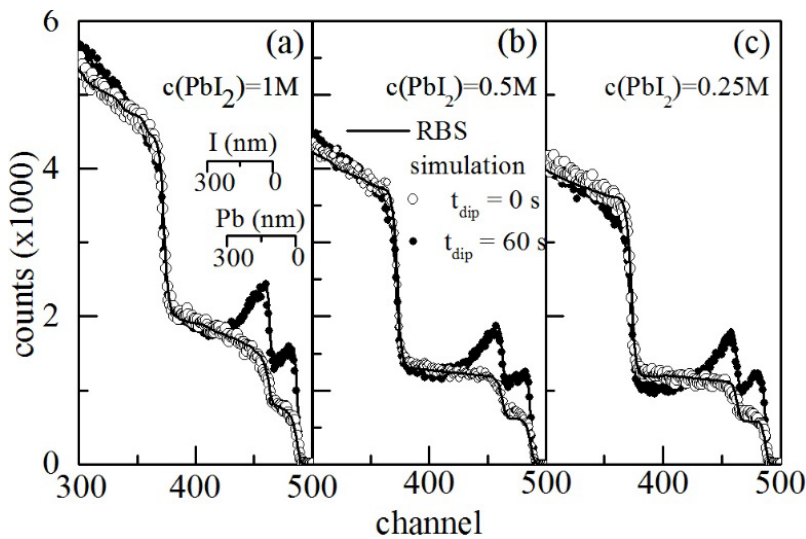


Figure 6: Rutherford backscattering spectra of model system $\text{np-TiO}_2/\text{PbI}_2$ (open circles) and $\text{np-TiO}_2/\text{CH}_3\text{NH}_3\text{PbI}_3$ (filled circles) for fixed dipping time of 60 s under variation of $c(\text{PbI}_2)$: (a) $c(\text{PbI}_2) = 1$ M, (b) $c(\text{PbI}_2) = 0.5$ M and (c) $c(\text{PbI}_2) = 0.25$ M. Solid lines present simulations using the multi-layer system as shown in Figure 7. Used geometry: (i)

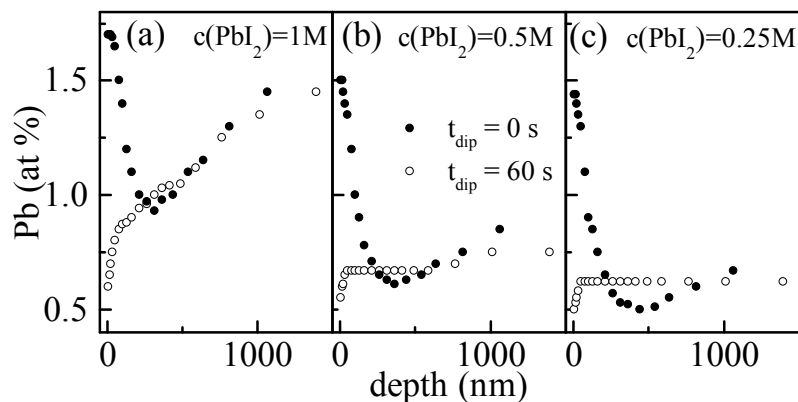


Figure 7: Lead concentration depth profile for optimized multi-layer system $\text{np-TiO}_2/\text{PbI}_2$ (open circles) and $\text{np-TiO}_2/\text{CH}_3\text{NH}_3\text{PbI}_3$ (filled circles) for fixed dipping time of 60 s and variation of $c(\text{PbI}_2)$: (a) $c(\text{PbI}_2) = 1$ M, (b) $c(\text{PbI}_2) = 0.5$ M and (c) $c(\text{PbI}_2) = 0.25$ M.

3.3.3 Effective Diffusion of Pb during Phase Transformation

The observed concentration profile was caused by mass transport, and cannot be described within an intercalation model as proposed by [29]. Comparing the effective ion radii of $r(\text{Pb}^{2+}) = 119 \text{ pm}$ [47] and $r(\text{CH}_3\text{NH}_3\text{I}^+) = 180 \text{ pm}$ [47], the observed faster Pb diffusion is logic, assuming $D \sim 1/r$ (Stokes-Einstein equation). Two regimes and/or processes were separated: accumulation at the surface and depletion in a certain depth. For better understanding, a simple 1D diffusion model was used [48]. First, depletion of Pb in a depth around 400 nm was considered with a Pb diffusion term (concentration $C1$ and diffusion coefficient $D1^{\text{Pb}}$) from the bulk (with certain initial concentration) to an infinite sink at the interface between organic precursor solution and sample. The assumed infinite sink was based on the dipping process, supplying an infinite source of $\text{CH}_3\text{NH}_3\text{I}$ providing a driving force for the reaction to $\text{CH}_3\text{NH}_3\text{PbI}_3$. Second, Pb reaching the sink was transformed into $\text{CH}_3\text{NH}_3\text{PbI}_3$ being an energetically favored reaction resulting in the observed surface crystallites. The consequent frazzling of the surface was considered in a second diffusion term (concentration $C2$ and diffusion coefficient $D2^{\text{eff}}$). A rigorous simplification with appropriate initial and boundary conditions made numerical simulation possible. Fick's second law of diffusion was used to obtain the simple recursion formalism:

$$C1_i^j = C1_i^{j-1} + D1^{\text{Pb}} \cdot \frac{\Delta t}{\Delta x^2} \cdot (C1_{i+1}^{j-1} - 2 \cdot C1_i^{j-1} + C1_{i-1}^{j-1}) \quad (1)$$

$$C2_i^j = C2_i^{j-1} + D2^{\text{eff}} \cdot \frac{\Delta t}{\Delta x^2} \cdot (C2_{i+1}^{j-1} - 2 \cdot C2_i^{j-1} + C2_{i-1}^{j-1}) \quad (2)$$

Time and space were discretized as Δt and Δx with j and i being the corresponding indices. Convergence was achieved for sufficiently small $\Delta t \ll \Delta x^2/D$. Used boundary conditions for the infinite sink and the $\text{CH}_3\text{NH}_3\text{PbI}_3$ conversion were:

$$B_{\text{conversion}} : C2_0^{j+1} = C1_0^j \quad (3)$$

$$B_{\text{sink}} : C1_0^j = 0 \quad (4)$$

$D1^{\text{Pb,eff}}$ and $D2^{\text{Pb,eff}}$ were optimized within an implemented least square fitting to the concentration profile data. $D1^{\text{Pb,eff}}$ corresponds to an effective diffusion of Pb within the nanocomposite. $D2^{\text{eff}}$ can be understood as a parameter (with unit of a diffusion coefficient) describing the $\text{CH}_3\text{NH}_3\text{PbI}_3$ crystallisation and the frazzling of the surface.

First, investigations were focused on the intermediate influence of the found reaction parameters t_1 and t_2 . Therefore Figure 8 (a) shows additional RBS spectra for dipping times of $t_{\text{dip}} = 5 \text{ s}$ and $t_{\text{dip}} = 20 \text{ s}$ for $c(\text{PbI}_2) = 0.5 \text{ M}$, measured in RBS geometry (ii). Figure 8 (b) compares obtained Pb concentration for $t_{\text{dip}} = 5 \text{ s}$, 20 s and 60 s . Diffusion simulation was performed optimizing $D1^{\text{Pb,eff}}$, $D2^{\text{Pb,eff}}$ and an initial Pb concentration (depth independent). The optimized diffusion coefficients were: $D1^{\text{Pb,eff}} = 3.7 \cdot 10^{-11} \text{ cm}^2/\text{s}$, $2.1 \cdot 10^{-11} \text{ cm}^2/\text{s}$, $1.0 \cdot 10^{-11} \text{ cm}^2/\text{s}$ and $D2^{\text{eff}} = 19.6 \cdot 10^{-10} \text{ cm}^2/\text{s}$, $7.5 \cdot 10^{-10} \text{ cm}^2/\text{s}$, and $2.5 \cdot 10^{-10} \text{ cm}^2/\text{s}$ for $t_{\text{dip}} = 5 \text{ s}$, 20 s and 60 s respectively. With increasing dipping time $D1^{\text{Pb,eff}}$ dropped by a factor of 4, first, and $D2^{\text{Pb,eff}}$ dropped almost a factor of 10, second. Both processes slowed down during the $\text{CH}_3\text{NH}_3\text{PbI}_3$

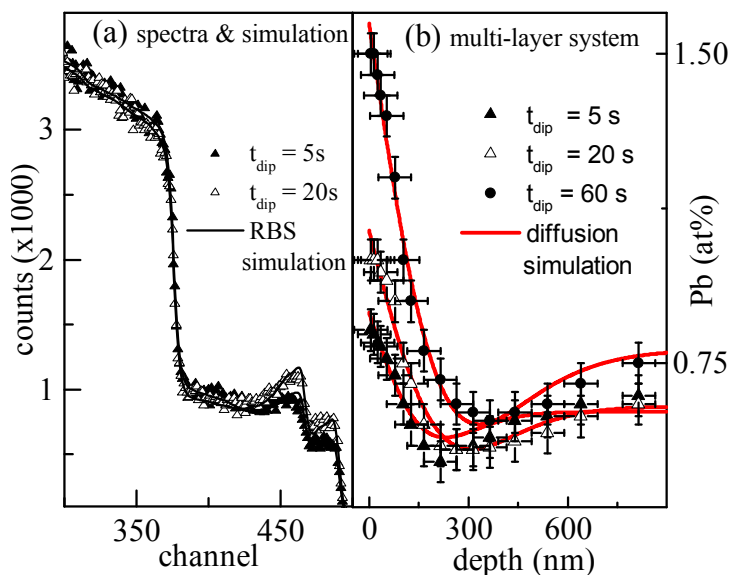


Figure 8: (a) RBS spectra for $\text{np-TiO}_2/\text{CH}_3\text{NH}_3\text{PbI}_3$ as obtained with from $c(\text{PbI}_2) = 0.5 \text{ M}$ using a dipping time of 5 and 20 s. (b) corresponding Pb concentration as obtained from multi-layer system for 0,5,20 and 60 s. Used geometry: (ii).

formation. The finding is in coincidence with the kinetic behaviour observed in the absorbance spectra, Figure 2. As remark, dipping time might deviate from reaction time due to rinsing and interruption by hand.

It has to be noted that spectra in Figure 6 were based on identical substrates, broken after PbI_2 spin coating and annealing, whereas the time dependence shown in Figure 8 was based on various samples. The found offset of the Pb concentration for a depth > 600 nm is attributed to a variability of initial PbI_2 infiltration in the fast spin coating process of the 70°C hot PbI_2 solution.

Figure 9 shows simulated concentration profiles as well as the optimized multi-layer system as obtained from RBS simulation for various PbI_2 concentrations of 1 M (a), 0.5 M (b) and 0.25 M (c) at the fixed dipping time of $t_{\text{dip}} = 60$ s. The depth dependent Pb concentration for $t_{\text{dip}} = 0$ s as shown in Figure 7 was hereby used as starting point in the simulation.

Optimized diffusion coefficients were: $D1^{\text{Pb,eff}} = 1.7 \cdot 10^{-11} \text{ cm}^2/\text{s}$, $1.6 \cdot 10^{-11} \text{ cm}^2/\text{s}$, $1.4 \cdot 10^{-11} \text{ cm}^2/\text{s}$ and $D2^{\text{Pb,eff}} = 3.0 \cdot 10^{-11} \text{ cm}^2/\text{s}$, $3.2 \cdot 10^{-11} \text{ cm}^2/\text{s}$, and $4.3 \cdot 10^{-11} \text{ cm}^2/\text{s}$ for $c(\text{PbI}_2) = 1$ M (a), 0.5 M (b) and 0.25 M respectively. Both effective diffusion coefficients were found to be independent of $c(\text{PbI}_2)$. For $D1^{\text{Pb}}$ it can be written:

$$D1^{\text{Pb}} \approx (1.5 \pm 0.5) \cdot 10^{-11} \frac{\text{cm}^2}{\text{s}} \quad (5)$$

This value is orders of magnitude lower than ionic diffusion of Pb^{2+} in water $D^{\text{Pb}^{2+}}_{\text{water}} \approx 2.2 \cdot 10^{-5} \text{ cm}^2/\text{s}$ [49] and orders of magnitude larger than reported diffusion of lead in zircon or apatite, where D ranges from $10^{-22} \text{ cm}^2/\text{s}$ to $10^{-14} \text{ cm}^2/\text{s}$ depending on temperature [50,51]. Compared

with Cu diffusion in In_2S_3 within the same np-TiO₂ host ($D^{\text{In}_2\text{S}_3}_{\text{Cu}} \approx 10^{-14} \text{ cm}^2/\text{s}$) [48] the lead diffusion coefficient here is three orders of magnitude larger. The parameter considering frazzling of the surface was approximated to $D2^{\text{eff}} = (3 \pm 1) \cdot 10^{-10} \text{ cm}^2/\text{s}$.

As remark, the applied 1D diffusion model was based on a rigorous planar simplification. However, it allowed an estimation of the effective 1D diffusion constants and provided some fundamental understanding. It has to be mentioned that a 1D model is rather speculative in the sense that mass transport via additional channels in 3D structures cannot be excluded. The development of such a 3D model for mass transport within the np-TiO₂ host sensitized with PbI_2 and dipped in $\text{CH}_3\text{NH}_3\text{I}$ solution seems not realistic to date. In addition, the detailed description of the time dependent diffusion constants would require the consideration of $\text{CH}_3\text{NH}_3\text{PbI}_3$ layer and/or crystallite formation and their influence on reaction dynamics as well as on the solution/sample interface.

4 Conclusion

The transformation of PbI_2 into $\text{CH}_3\text{NH}_3\text{PbI}_3$ was studied based on depth dependent concentration profiles from complementary techniques EDX and RBS with orthogonal analysis beam direction. After transformation, the lead concentration profile showed a pronounced enrichment at the surface and a depletion in a certain depth caused by mass transport during $\text{CH}_3\text{NH}_3\text{PbI}_3$ transformation. The $\text{CH}_3\text{NH}_3\text{PbI}_3$ transformation mechanism therefore is based on an insertion reaction of the organic component into the layered PbI_2 [7,18,29] and a second process related

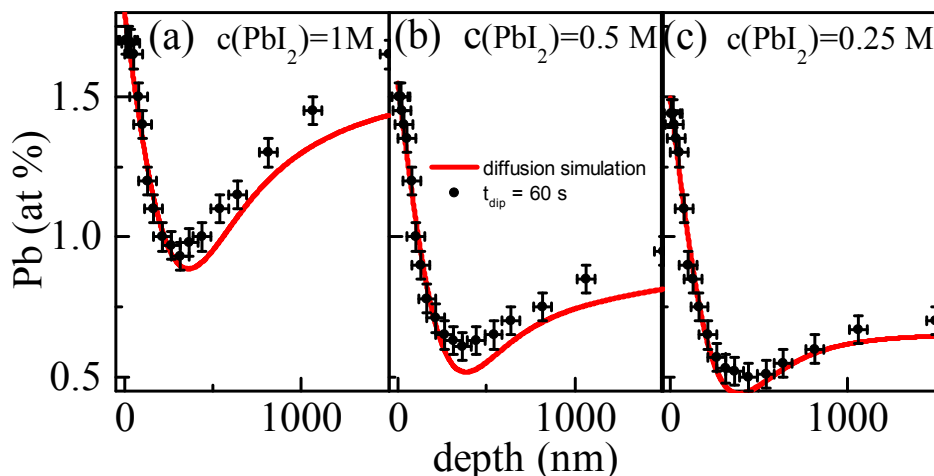


Figure 9: Simulation of effective lead diffusion by transformation within the np-TiO₂ host for a fixed dipping time of $t_{\text{dip}} = 60$ s under variation of $c(\text{PbI}_2) = 1$ M (a), 0.5 M (b) and 0.25 M (c). Optimization of $D1^{\text{Pb,eff}}$, $D2^{\text{Pb,eff}}$.

to diffusion of Pb within the nanocomposite towards the sample/solution interface. The diffusion of Pb seems to be a limiting process in the phase transformation. We believe this process allows the formation of $\text{CH}_3\text{NH}_3\text{PbI}_3$ from stacked PbI_2 and $\text{CH}_3\text{NH}_3\text{I}$ by inter-diffusion, as reported by [52]. An effective Pb diffusion constant was estimated to about $(1.5 \pm 0.5) \cdot 10^{-11} \text{ cm}^2/\text{s}$, using a rigorous simplified 1D diffusion model. $\text{CH}_3\text{NH}_3\text{PbI}_3$ was found to be instant unstable against $^4\text{He}^+$ radiation. For comparison, thin film solar cell absorbers such as $\text{Cu}(\text{In,Ga})\text{Se}_2$ [53] are superior regarding radiation hardness. A detailed analysis of ion track evolution and $\text{CH}_3\text{NH}_3\text{PbI}_3$ degradation, however, was impossible due to opposing demands on measurement statistics and degradation. For future RBS measurements, a strongly increased detector area and expanded ion beams are recommended in order to get more detailed information about degradation of $\text{CH}_3\text{NH}_3\text{PbI}_3$.

Acknowledgements: The authors appreciate E. Wendler from the Friedrich-Schiller-Universität Jena, Institut für Festkörperphysik for the possibility to perform RBS measurements at the 'JULIA' tandem accelerator, U. Barth for assistance and support during RBS measurements and U. Jerol from HZB, Institut für Silizium Photovoltaik for support with $\text{CH}_3\text{NH}_3\text{I}$ synthesis. V. Somsongkul is grateful to the Department of Materials Science, Faculty of Science, Kasetsart University for funding a research stay at the HZB.

References

- [1] Baikie, T., Fang, Y., Kadro, J.M., Schreyer, M., Wei, F., Mhaisalkar, S.G., et al., Synthesis and crystal chemistry of the hybrid perovskite $(\text{CH}_3\text{NH}_3)\text{PbI}_3$ for solid-state sensitised solar cell applications. , *J. Mater. Chem. A* , 2013, 1, 5628–5641.
- [2] Yamada, Y., Nakamura, T., Endo, M., Wakamiya, A., Kanemitsu, Y., Near-band-edge optical responses of solution-processed organic–inorganic hybrid perovskite $\text{CH}_3\text{NH}_3\text{PbI}_3$ on mesoporous TiO_2 electrodes. , *Appl. Phys. Express* , 2014, 7, 32302–32305.
- [3] Xing, G., Mathews, N., Lim, S.S., Yantara, N., Liu, X., Sabba, D., et al., Low-temperature solution-processed wavelength-tunable perovskites for lasing. , *Nat. Mater.* , 2014, 13, 476–480.
- [4] Xing, G., Mathews, N., Sun, S., Lim, S.S., Lam, Y.M., Grätzel, M., et al., Long-range balanced electron- and hole-transport lengths in organic-inorganic $\text{CH}_3\text{NH}_3\text{PbI}_3$. , *Science* , 2013, 342, 344–351.
- [5] Stranks, S.D., Eperon, G.E., Grancini, G., Menelaou, C., Alcocer, M.J.P., Leijtens, T., et al., Electron-hole diffusion lengths exceeding 1 micrometer in an organometal trihalide perovskite absorber. , *Science* , 2013, 342, 341–344.
- [6] Kojima, A., Teshima, K., Shirai, Y., Miyasaka, T., Organometal halide perovskites as visible-light sensitizers for photovoltaic cells. , *J. Am. Chem. Soc.* , 2009, 131, 6050–6051.
- [7] Burschka, J., Pellet, N., Moon, S.-J., Humphry-Baker, R., Gao, P., Nazeeruddin, M.K., et al., Sequential deposition as a route to high-performance perovskite-sensitized solar cells. , *Nature* , 2013, 499, 316–319.
- [8] Liu, D., Kelly, T.L., Perovskite solar cells with a planar hetero-junction structure prepared using room-temperature solution processing techniques. , *Nat. Photonics* , 2013, 8, 133–138.
- [9] Jeon, N.J., Noh, J.H., Kim, Y.C., Yang, W.S., Ryu, S., Seok, S. II, Solvent engineering for high-performance inorganic-organic hybrid perovskite solar cells. , *Nat. Mater.* , 2014, 13, 897–903.
- [10] NREL, Research Cell Efficiency Records , 2014, <http://www.nrel.gov/ncpv/>.
- [11] Mitzi, D., Dimitrakopoulos, C.D., Kosbar, L.L., Organic-inorganic electronic devices based on hybrid perovskites. , *Device Res. Conf.* , 2001, 467, 185–186.
- [12] Eperon, G.E., Burlakov, V.M., Docampo, P., Goriely, A., Snaith, H.J., Morphological Control for High Performance, Solution-Processed Planar Heterojunction Perovskite Solar Cells. , *Adv. Funct. Mater.* , 2014, 24, 151–157.
- [13] Jeon, N.J., Lee, H.G., Kim, Y.C., Seo, J., Noh, J.H., Lee, J., et al., o-Methoxy substituents in spiro-OMeTAD for efficient inorganic-organic hybrid perovskite solar cells. , *J. Am. Chem. Soc.* , 2014, 136, 7837–7840.
- [14] Ball, J.M., Lee, M.M., Hey, A., Snaith, H.J., Low-temperature processed meso-superstructured to thin-film perovskite solar cells. , *Energy Environ. Sci.* , 2013, 6, 1739–1743.
- [15] Carnie, M.J., Charbonneau, C., Davies, M.L., Troughton, J., Watson, T.M., Wojciechowski, K., et al., A one-step low temperature processing route for organolead halide perovskite solar cells. , *Chem. Commun. (Camb)* , 2013, 49, 7893–7895.
- [16] Eperon, G.E., Burlakov, V.M., Goriely, A., Snaith, H.J., Neutral color semitransparent microstructured perovskite solar cells. , *ACS Nano* , 2014, 8, 591–598.
- [17] Roldán-Carmona, C., Malinkiewicz, O., Soriano, A., Mínguez Espallargas, G., Garcia, A., Reinecke, P., et al., Flexible high efficiency perovskite solar cells. , *Energy Environ. Sci.* , 2014, 7, 994–998.
- [18] Liang, K., Mitzi, D.B., Prikas, M.T., Synthesis and Characterization of Organic–Inorganic Perovskite Thin Films Prepared Using a Versatile Two-Step Dipping Technique. , *Chem. Mater.* , 1998, 10, 403–411.
- [19] Yongzhen, W., Islam, A., Yang, X., Qin, C., Liu, J., Zhang, K., et al., Retarding the crystallization of PbI_2 for highly reproducible planar-structured perovskite solar cells via sequential deposition. , *Energy Environ. Sci.* , 2014, 7, 2934–2938.
- [20] Ma, Y., Zheng, L., Chung, Y.-H., Chu, S., Xiao, L., Chen, Z., et al., A highly efficient mesoscopic solar cell based on $\text{CH}_3\text{NH}_3\text{PbI}_3\text{-xCl}_x$ fabricated via sequential solution deposition. , *Chem. Commun. (Camb)* , 2014, 50, 12458–61.
- [21] Barrows, A., Pearson, A., Kwak, C., Dunbar, A., Buckley, A., Lidzey, D., Efficient planar heterojunction mixed-halide perovskite solar cells deposited via spray-deposition. , *Energy Environ. Sci.* , 2014, 7, 2944–2950.
- [22] Chen, Q., Zhou, H., Hong, Z., Luo, S., Duan, H.-S., Wang, H.-H., et al., Planar heterojunction perovskite solar cells via vapor-assisted solution process. , *J. Am. Chem. Soc.* , 2014, 136, 622–625.
- [23] Im, J.-H., Kim, H.-S., Park, N.-G., Morphology-photovoltaic property correlation in perovskite solar cells: One-step versus

- two-step deposition of CH₃NH₃PbI₃, *APL Mater.*, 2014, 2, 081510–081518.
- [24] Stoumpos, C.C., Malliakas, C.D., Kanatzidis, M.G., Semiconducting tin and lead iodide perovskites with organic cations: phase transitions, high mobilities, and near-infrared photoluminescent properties., *Inorg. Chem.*, 2013, 52, 9019–9038.
- [25] De Bastiani, M., D'Innocenzo, V., Stranks, S.D., Snaith, H.J., Petrozza, A., Role of the crystallization substrate on the photoluminescence properties of organo-lead mixed halides perovskites., *Apl Mater.*, 2014, 2, 081509–081515.
- [26] Supasai, T., Rujisamphan, N., Ullrich, K., Chemseddine, A., Dittrich, T., Formation of a passivating CH₃NH₃PbI₃/PbI₂ interface during moderate heating of CH₃NH₃PbI₃ layers., *Appl. Phys. Lett.*, 2013, 103, 183906–183909.
- [27] Somsongkul, V., Lang, F., Jeong, A.R., Rusu, M., Arunchaiya, M., Dittrich, T., Hole blocking Pbl₂/CH₃NH₃Pbl₃ interface., *Phys. status solidi - Rapid Res. Lett.*, 2014, 08, 763–766.
- [28] Chen, Q., Zhou, H., Song, T.-B., Luo, S., Hong, Z., Duan, H.-S., et al., Controllable Self-Induced Passivation of Hybrid Lead Iodide Perovskites toward High Performance Solar Cells., *Nano Lett.*, 2014, 14, 4158–4163.
- [29] Ahmad, S., Kanaujia, P.K., Niu, W., Baumberg, J.J., Vijaya Prakash, G., In situ intercalation dynamics in inorganic-organic layered perovskite thin films., *ACS Appl. Mater. Interfaces*, 2014, 6, 10238–10247.
- [30] Dwivedi, V.K., Vijaya Prakash, G., Fabrication and room-temperature exciton photoluminescence stability studies of inorganic–organic hybrid (C₁₂H₂₅NH₃)₂SnI₄ thin films., *Solid State Sci.*, 2014, 27, 60–64.
- [31] Cheng, Z., Lin, J., Layered organic–inorganic hybrid perovskites: structure, optical properties, film preparation, patterning and templating engineering., *CrystEngComm*, 2010, 12, 2646–2662.
- [32] Frost, J.M., Butler, K.T., Brivio, F., Hendon, C.H., van Schilfhaarde, M., Walsh, A., Atomistic origins of high-performance in hybrid halide perovskite solar cells., *Nano Lett.*, 2014, 14, 2584–2590.
- [33] Tan, K.W., Moore, D.T., Saliba, M., Sai, H., Estroff, L. a., Hanrath, T., et al., Thermally induced structural evolution and performance of mesoporous block copolymer-directed alumina perovskite solar cells., *ACS Nano*, 2014, 8, 4730–4739.
- [34] Etgar, L., Gao, P., Xue, Z., Peng, Q., Chandiran, A.K., Bin, L., et al., Mesoscopic CH₃NH₃PbI₃/TiO₂ heterojunction solar cells., *J. Am. Chem. Soc.*, 2012, 134, 17396–17399.
- [35] Metzner, H., Hahn, T., Gossila, M., Conrad, J., Bremer, J.-H., Rutherford backscattering spectroscopy of rough films: Experimental aspects., *Nucl. Instruments Methods Phys. Res. Sect. B Beam Interact. with Mater. Atoms*, 1998, 134, 249–261.
- [36] Mayer, M., Toussaint, U. Von, Dewalque, J., Dubreuil, O., Henrist, C., Cloots, R., et al., Nuclear Instruments and Methods in Physics Research B Rutherford backscattering analysis of porous thin TiO₂ films., *Nucl. Inst. Methods Phys. Res. B*, 2012, 273, 83–87.
- [37] Lund, J., Shah, K., Squillante, M., Properties of lead iodide semiconductor radiation detectors., *Nucl. Instruments Methods Phys. Res. Sect. A Accel. Spectrometers, Detect. Assoc. Equip.*, 1989, 283, 299–302.
- [38] Kulkarni, S.A., Baikie, T., Boix, P.P., Yantara, N., Mathews, N., Mhaisalkar, S., Band-gap tuning of lead halide perovskites using a sequential deposition process., *J. Mater. Chem. A*, 2014, 2, 9221–9225.
- [39] Yella, A., Heiniger, L.-P., Gao, P., Nazeeruddin, M.K., Grätzel, M., Nanocrystalline rutile electron extraction layer enables low-temperature solution processed perovskite photovoltaics with 13.7% efficiency., *Nano Lett.*, 2014, 14, 2591–2596.
- [40] Li, N., Dong, H., Dong, H., Li, J., Li, W., Niu, G., et al., Multifunctional perovskite capping layers in hybrid solar cells., *J. Mater. Chem. A*, 2014, 2, 14973–14978.
- [41] Schiwietz, G., Czerski, K., Roth, M., Staufenbiel, F., Grande, P.L., Femtosecond dynamics – snapshots of the early ion-track evolution., *Nucl. Instruments Methods Phys. Res. Sect. B Beam Interact. with Mater. Atoms*, 2004, 226, 683–704.
- [42] Murat, M., Akkerman, A., Barak, J., Ion track structure and dynamics in SiO₂., *9th Eur. Conf. Radiat. Its Eff. Components Syst. (10-14 Sept. 2007, Deauville, Fr)*, IEEE, 2007, 1–9.
- [43] Balanzat, E., Betz, N., Bouffard, S., Swift heavy ion modification of polymers., *Nucl. Instruments Methods Phys. Res. Sect. B Beam Interact. with Mater. Atoms*, 1995, 105, 46–54.
- [44] Ackermann, J., Angert, N., Neumann, R., Trautmann, C., Dischner, M., Hagen, T., et al., Ion track diameters in mica studied with scanning force microscopy., *Nucl. Instruments Methods Phys. Res. Sect. B Beam Interact. with Mater. Atoms*, 1996, 107, 181–184.
- [45] Ziegler, J.F., Ziegler, M.D., Biersack, J.P., SRIM – The stopping and range of ions in matter (2010)., *Nucl. Instruments Methods Phys. Res. Sect. B Beam Interact. with Mater. Atoms*, 2010, 268, 1818–1823.
- [46] Jäger, W., Roth, J., Microstructure of Ni and stainless steel after multiple energy He and D implantation., *J. Nucl. Mater.*, 1980, 94, 756–766.
- [47] Kim, H.-S., Im, S.H., Park, N.-G., Organolead Halide Perovskite: New Horizons in Solar Cell Research., *J. Phys. Chem. C*, 2014, 118, 5615–5625.
- [48] Juma, A.O., Pistor, P., Fengler, S., Dittrich, T., Wendler, E., Copper diffusion in thin In₂S₃ layers investigated by Rutherford Backscattering Spectroscopy., *Thin Solid Films*, 2012, 520, 6740–6743.
- [49] SATO, H., YUI, M., YOSHIKAWA, H., Ionic Diffusion Coefficients of Cs⁺, Pb²⁺, Sm³⁺, Ni²⁺, SeO₂ and TcO₄ in Free Water Determined from Conductivity Measurements., *J. Nucl. Sci. Technol.*, 1996, 33, 950–955.
- [50] Cherniak, D., Watson, E., Pb diffusion in zircon., *Chem. Geol.*, 2001, 172, 5–24.
- [51] Cherniak, D., Lanford, W., Ryerson, F., Lead diffusion in apatite and zircon using ion implantation and Rutherford Backscattering techniques., *Geochim. Cosmochim. Acta*, 1991, 55, 1663–1673.
- [52] Xiao, Z., Bi, C., Shao, Y., Dong, Q., Wang, Q., Yuan, Y., et al., Efficient, high yield perovskite photovoltaic devices grown by interdiffusion of solution-processed precursor stacking layers., *Energy Environ. Sci.*, 2014, 7, 2619–2623.
- [53] Otte, K., Makhova, L., Braun, A., Kononov, I., Flexible Cu(In,Ga)Se₂ thin-film solar cells for space application., *Thin Solid Films*, 2006, 511-512, 613–622.